APL Materials

Ferroelectric/multiferroic self-assembled vertically aligned nanocomposites: Current and future status

Cite as: APL Mater. **9**, 030904 (2021); https://doi.org/10.1063/5.0035366
Submitted: 28 October 2020 . Accepted: 28 January 2021 . Published Online: 10 March 2021

Oon Jew Lee, Shikhar Misra, Haiyan Wang, and J. L. MacManus-Driscoll

Ferroelectric/multiferroic self-assembled vertically aligned nanocomposites: Current and future status

Cite as: APL Mater. 9, 030904 (2021); doi: 10.1063/5.0035366
Submitted: 28 October 2020 • Accepted: 28 January 2021 •
Published Online: 10 March 2021

Oon Jew Lee,[1,a)] Shikhar Misra,[2] Haiyan Wang,[2,3] and J. L. MacManus-Driscoll[4]

AFFILIATIONS

[1] Faculty of Science and Marine Environment, Universiti Malaysia Terengganu, 21030 Kuala Nerus, Malaysia
[2] School of Materials Engineering, Purdue University, West Lafayette, Indiana 47907, USA
[3] School of Electrical and Computer Engineering, Purdue University, West Lafayette, Indiana 47907, USA
[4] Department of Materials Science and Metallurgy, University of Cambridge, 27 Charles Babbage Rd., Cambridge CB3 OFS, United Kingdom

Note: This paper is part of the Special Topic on 100 Years of Ferroelectricity—A Celebration.
[a)] **Author to whom correspondence should be addressed:** oonjew@umt.edu.my

ABSTRACT

Even a century after the discovery of ferroelectricity, the quest for the novel multifunctionalities in ferroelectric and multiferroics continues unbounded. Vertically aligned nanocomposites (VANs) offer a new avenue toward improved (multi)functionality, both for fundamental understanding and for real-world applications. In these systems, vertical strain effects, interfaces, and defects serve as key driving forces to tune properties in very positive ways. In this Perspective, the twists and turns in the development of ferroelectric/multiferroics oxide–oxide and unconventional metal–oxide VANs are highlighted. In addition, the future trends and challenges to improve classic ferroelectric/multiferroic VANs are presented, with emphasis on the enhanced functionalities offered by existing VANs, as well as those in emerging systems.

I. INTRODUCTION

Complex metal oxides offer a spectrum of tunable functionalities, including ferroelectricity, ferromagnetism, magnetoelectric (ME), superconductivity, ionic conductivity, dielectricity, and plasmonic resonance.[1–7] Incorporating complex metal oxides into vertically aligned nanocomposite (VAN) thin films provides another handle to tune properties in very positive ways. Improved functionalities of these complex metal oxides are realized and coupling between different functions in the composite films induces novel multi-functionalities.[8]

Of all the aforementioned functionalities, the phenomenon of ferroelectricity is of high topical interest. Ferroelectric materials have constantly attracted scientific interest owing to their switchable spontaneous electric polarization by an electric field application.[9] Apart from spontaneous polarization switching, they also exhibit piezoelectric, pyroelectric, dielectric, and electro-optic properties,[10] and this is only the start. When ferroelectric research is further extended to include magnetic coupling, hence producing multiferroicity, this further degree of freedom is highly promising for yet more technological applications. Both ferroelectrics and multiferroics have been widely investigated for countless applications such as supercapacitors, efficient energy harvesting and storage, ultralow power logic-memory devices, high power electronic transducers, solid state electrocaloric cooling/heating devices, microwave electronics, and non-volatile memories.[5,11–13] As part of the drive toward device miniaturization, the unique VAN architecture has improved the existing functionalities in a transformative way, beyond the state-of-the-art ferroelectrics such as $Pb_{1-x}Zr_xTiO_3$.[14]

This article begins with a short overview of VANs (their possible structures and proven salient properties) and is followed by the early works of ferroelectric/multiferroic VANs. Then, recent advances of oxide–oxide and unconventional metal–oxide ferroelectric/multiferroic VANs are highlighted. Finally, their future perspective and challenges are outlined.

II. THE ANATOMY OF VANS

VANs are self-assembled nanostructures in which two immiscible phases grow epitaxially on the substrate. Fabrication of VANs is made easy via physical thin film deposition methods. Both templated growth and spontaneous ordered growth can occur.[6,8] The former involves the utilization of templating methods such as anodic aluminum oxide (AAO) templates,[15] block copolymers,[16] lithography,[17] and focus ion beams.[18,19] Spontaneous growth offers synergistic advantages to control deposition precisely, minimize defects, and overcome the complication of templated growth that implies extra step of template removal.[20] Hence, the spontaneous growth is rather facile and low-cost and hence favorable for device integration.

With proper selection, the host matrix nucleates and grows epitaxially on the crystallographically matched substrate. The host and epiphyte phases are vertically coupled through an epitaxial relationship or through domain matching epitaxy (DME).[7] Figure 1 shows that three dimensional (3D) VANs are comprised of diverse patterns with tunable shape, size, and distribution. Their diversity is reflected in various structures such as circular nanocolumn matrix, facet nanocolumn matrix, nanomazes, and nanocheckerboard. In the most typical configuration, one phase (the one closely structurally matched with the substrate) forms the matrix phase, and the other forms pseudo-1D nanopillars or nanodomains (such as circular, rectangular, pyramidal, hexagonal, octagonal, and triangular shapes[1,6,20]) embedded in the matrix [Figs. 1(a) and 1(c)]. This structure is referred to as the 1–3 configuration and is the most commonly used one. The growth origin of 1–3 configurations is driven by the minimization of the total free energy that depends on thermodynamic epitaxial stability, growth kinetics, and phase ratio.[1,8,21] According to phase field simulations,[1] competing interfacial interactions and elastic moduli that arise between matrix and embedded phases, as well as the interaction of these phases with the substrate, are vital. It is found that circular pillars with small diameters minimize the surface energy. On the other hand, the elastic strain energy is dominant in the case of faceted domain nanopillars.[1] The phase has a higher interfacial energy (lower wettability) on the substrate such that it nucleates and grows into nanopillars. The other phase, with a lower interfacial energy, undergoes layer-by-layer growth and becomes the planar matrix.[21] Beyond a critical thickness of ~20 nm (above which the role of the substrate is strongly diminished), the stiffer phase in the film dominates the strain of softer phase.[22]

Depending on the epitaxial stability consideration, the role of each phase as the matrix and pillar can be reversed when grown on differently oriented substrates. For instance, the $CoFe_2O_4$ (CFO) phase in BFO–$CoFe_2O_4$ (BFO–CFO) VANs evolves from faceted pyramidal nanodomains and subsequently formed into nanomaze structures on (001), (111), and (110) $SrTiO_3$ (STO) substrates.[20] In addition, growth kinetics and phase ratios are the key factors in tuning the feature size of nanodomains, phase segregation, and stoichiometry of VANs.[1,23] As a result, smaller nanodomains merge into belt-shaped or T-shaped nanostructures, as observed in the nanomaze morphology [Fig. 1(d)].[21]

On the contrary, nanocheckerboard VANs [Fig. 1(b)] originate from highly ordered (pseudo-) spinodal decomposition growth.[6,8] Again, the well-matched crystallography and sufficient growth kinetics between the decomposing phases and substrate are prerequisites for the formation of nanocheckerboards.[20]

Depending on the overall film thickness, VANs display higher interface-to-volume ratio by up to two orders of magnitude[22] as compared to the conventional multilayer counterparts of the 2–2 configuration [Fig. 1(e)]. Unlike the lateral thin films, the strain exerted by a substrate has inherent limitation owing to their critical film thickness of a few tens of nm. The 1D nanopillars in the VANs, on the other hand, extend perpendicularly throughout the entire thickness of the film, even up to the micrometer thickness.[22,24] Furthermore, for thinner films (<30 nm), the in-plane (IP) and

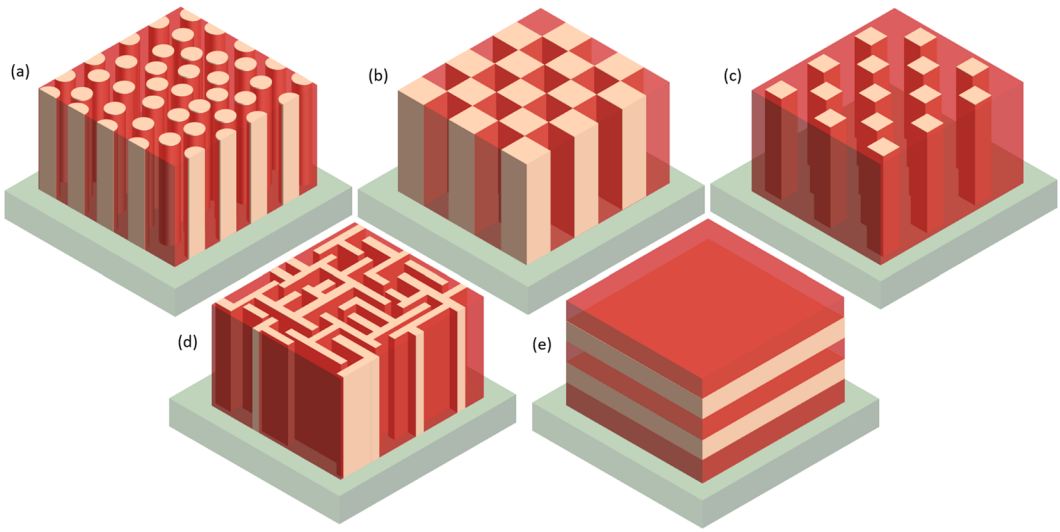

FIG. 1. 3D schematic illustration of vertical aligned nanocomposites (1–3 type) that comprise two immiscible constituents grown simultaneously on a substrate with (a) circular nanocolumn matrix, (b) nanocheckerboard (c) facet nanocolumn matrix, (d) nanomaze, and (e) conventional multilayer thin films (2–2 type).

out-of-plane (OP) strain in the VAN can be tuned independently via the separate lateral substrate and vertical pillar strain control mechanisms.[4] The high interface-to-volume ratio in addition to uniform strain control imparted by the fine dimensions of the structure[22] enables unprecedented possibilities to improve the physical properties of the VANs via strain-, interface-, and defect-control. Vertical strain engineering, stemming from lattice mismatch and elastic coupling, is critical to promote competing interactions among spin, charge, orbital, and lattice degrees of freedom, polarization domain, and magnetic moment.[1,10] Subsequently, these competing interactions are intimately coupled to ferroelectricity and multiferroic properties. Furthermore, the vertical heterointerfaces and defects (notably oxygen vacancies) in VANs also adversely affected the polarization, magnetoelectric coupling strength, and dielectric relaxation.[1,25] Hence, a delicate balance between the VAN morphology and the fundamental couplings is vital to expand the realm of potential multifunctionalities in ferroelectrics and multiferroics, as discussed in Sec. III.

III. OVERVIEW OF FERROELECTRIC/MULTIFERROICS AND PROPERTY ENHANCEMENTS OFFERED BY VANS

Extensive research has been focused on oxide–oxide based VAN thin films, with functionalities including ferromagnetic, ferroelectric, multiferroic, dielectric, semiconducting, superconducting, and nonlinear optical effects.[11,24,26–35] An overview of the property enhancements offered by VAN structures for tuning ferroelectrics whether used alone or coupled with ferromagnets in artificial magnetoelectrics is shown in Fig. 2. The property enhancements offered by ferroelectric VANs are shown, as well as the properties achieved in artificial multiferroic VANs, which incorporate ferroelectrics. In summary, by exploiting the enhanced property advantages offered by VAN architectures, ferroelectric VANs with enhanced Curie temperatures (T_cs),[24,36] lower leakage,[37,38] fine dimensions,[6,8] and higher polarization[12,39] offer the prospect of higher density nonvolatile random-access memory. The increased T_cs, higher temperature coefficient capacitance (TCC), and increased piezoelectric coefficients[12] offer the prospect of higher operation temperature Pb-free piezoelectrics for energy harvesting, actuation, and energy storage. In addition, the increased dielectric tunability without increasing the loss at the same time [or high commutation quality factor (CQF)][13,36] offers the prospect of improved tunable microwave filters. Both enhanced optical anisotropy responses in terms of dielectric permittivity and polarization offer the prospect of ultrasensitive and broadband optical sensors, signal processors, and lasers.[13,40,41]

Multiferroics underpin the emergence of more than one primary ferroic order, including ferromagnetism, ferroelectric, ferroelastic, and ferrotoroidic in a phase but also not limited to antiferromagnetism and magnetoelectricity.[5] The coexistence of ferromagnetic and ferroelectric orders is pivotal to induce electric polarization by an applied magnetic field or vice versa to mediate the magnetization through the electric field. However, these orders often exclude each other owing to their intrinsic electronic structure. Ferroelectricity relies on transition metals with empty *d* orbitals, whereas the magnetism involves partially filled *d* orbitals. Single-phase multiferroic materials such as $BiFeO_3$, $TbMnO_3$, and Cr_2O_3 are scarce in nature and do not offer large magnetoelectric effects at room temperature.[1,5] On the other hand, artificial multiferroics with moderate performance at room temperature can be made by combining ferroelectric and ferromagnetic (magnetostrictive) phases in a VAN architecture. Artificial multiferroic VANs offer exemplary characteristics with large magnetoelectric coefficients[42] and spin-driven room temperature ferroelectricity,[43] which are of great interests for non-volatile memory and energy harvesters with ultralow power (~100 mV).[5] The electric field induced ferromagnetic resonance characteristics[44] are also beneficial for tunable

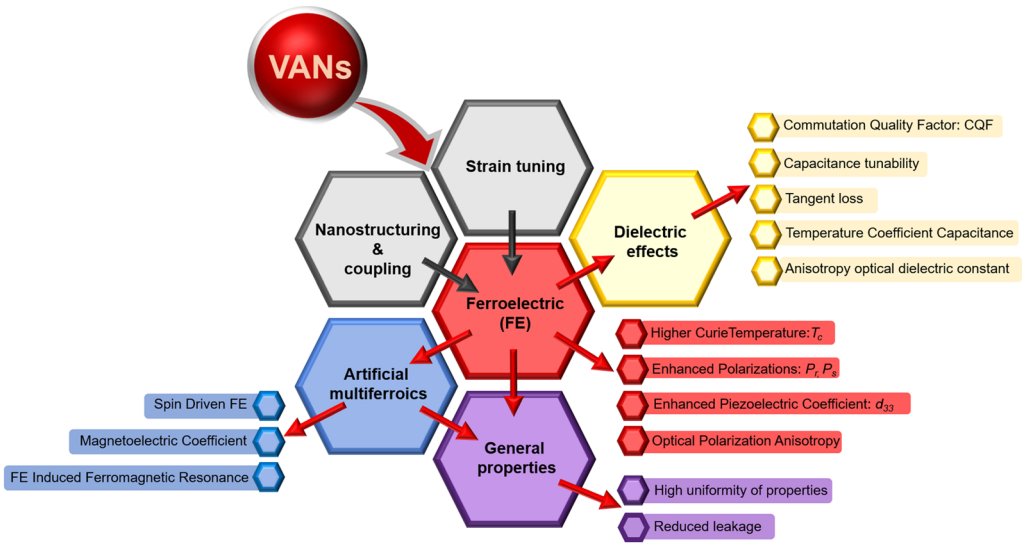

FIG. 2. Schematic representation of the main interactions (gray) that can take place in ferroelectric-based VAN systems leading to enhanced ferroelectric properties (red), improved dielectric properties (yellow), novel artificial multiferroics and effects when combined with magnetic systems (blue), and improved properties general to all systems (purple).

radiofrequency (RF)/microwave magnetic devices and resonators that rely on robust spontaneous polarization switching and tunable ferromagnetic resonance.

IV. EARLY WORKS ON CLASSIC FERROELECTRIC AND MULTIFERROIC VANS

There has been a considerable volume of work on ferroelectric and multiferroic VAN over the past 15 years. The earliest work on ferroelectric VAN focused on the classic ferroelectric, $BaTiO_3$–Sm_2O_3 (BTO–SmO). The stiffer SmO nanopillars exerted a >2% vertical tensile strain on the BTO phase, forcing the tetragonal structure of BTO to be maintained at a high temperature (up to 800 °C).[24] This also opened a path for the BTO–SmO VANs to work as piezoactuators, as an increased longitudinal piezoelectric coefficient (d_{33}) of 45 pm V^{-1}–50 pm V^{-1} was achieved up to 250 °C.[12] Additionally, owing to the unusual strain states induced in the BTO, a high transverse piezoelectric coefficient (d_{31}) was achieved,[12] outperforming the state-of-the-art $Pb_{1-x}Zr_xTiO_3$ films at > 200 pm V^{-1} (as tabulated in Table I). The leakage current of the BTO–SmO VANs was reduced by a factor of 15 because of the formation of highly crystalline BTO in the composite.[24] Li *et al.* suggested that both vertical strain and interfaces have active roles to trap oxygen vacancies (defects), which suppress the carrier mobility and trigger a trap-controlled space-charge-limited current (SCLC) mechanism in the BTO–SmO films.[25]

Similar enhancements in T_c from 130 °C to 616 °C and d_{33} of ~80 pmV^{-1} were observed in more recent studies on (111)-oriented BTO–SmO VANs that were grown on 0.5 wt. % Nb-doped (111) $SrTiO_3$ substrates.[45] The origin of enhanced ferroelectric and piezoelectric properties lies in the presence of unusual strain states also known as the auxetic-like effect. Such an auxetic-like effect is achieved because there is IP and OP expansion of the BTO matrix once the stiff SmO nanopillars shrink upon cooling.[8] $Ba_{0.6}Sr_{0.4}TiO_3$–Sm_2O_3 (BSTO–SmO) VANs also agree with the earlier BTO–SmO work that vertical strain induces strong enhancements of T_c and dielectric tunability, which scale inversely with the dielectric loss and leakage current. $BaTiO_3$–CeO_2 (BTO–CeO) VANs also show the similar behavior whereby both T_c and remnant polarization (P_r) are enhanced. Khatkhatay *et al.* reported a slightly enhanced T_c of 175 °C and saturation polarization (P_s) of 29 μC cm^{-2} in BTO–CeO_2, demonstrating a precise vertical strain tuning (tensile strain of 0.6%) by the CeO_2 nanopillar phase.[46]

TABLE I. Classic oxide–oxide ferroelectric and multiferroic VANs that have been developed.

VAN	System	Enhanced functionalities	References
	Classic ferroelectric oxide–oxide		
Circular nanocolumn-matrix	$BaTiO_3$–Sm_2O_3/Nb–STO (100)	• Increase T_c up to 800 °C •Increase d_{33} of 45–50 pmV^{-1} up to 250 °C • d_{31} exceeds PZT films at 200 pm V^{-1} • Reduce leakage current to 2.2 × 10^{-7} A cm^{-2}	12,24
	$Ba_{0.6}Sr_{0.4}TiO_3$–Sm_2O_3/SRO/STO (100)	• High tunability (75%) scales inversely with dielectric loss (0.01)	13
	$BaTiO_3$–CeO_2/SRO/STO (100) $BaTiO_3$–CeO_2/$SrRuO_3$/sto???n/Si	• Increase T_c up to 175 °C and 150 °C • Increase in remnant polarization up to 29 μC cm^{-2}	46
	BTO-NiO/Nb-STO (100)	• Enhancement of ~240% in the dielectric constant	95
	Classic multiferroic oxide–oxide		
Circular/Rectangular nanocolumn-Matrix	$BaTiO_3$–$CoFe_2O_4$/SRO/STO	• Achieved P_s of 23 μC cm^{-2} • Obtained d_{33} of 50 pm V^{-1} • Direct coupling between BTO and CFO	47,57
Nanocheckerboard	$BiFeO_3$–Sm_2O_3/Nb–STO (100)	• Reduced leakage current density of three orders of magnitude lower • Reduced the dielectric loss to 0.016	37,38
	$BiFeO_3$–Eu_2O_3/SRO/STO (100) $BiFeO_3$–$BaZrO_3$/SRO/STO (100)	• Reduced leakage current <1.25 $mAcm^{-2}$	49
Rectangular nanocolumn matrix	$BiFeO_3$–$CoFe_2O_4$/SRO/STO (100)	• Sharp 180° PFM domain switching in the BFO matrix with multiple wring–rewriting poling • ME coefficient of 20 mV cm^{-1} Oe^{-1} measured by a magnetic cantilever method	35,42

Looking now into the early works of the classic multiferroic VANs, Zheng *et al.* pioneered the fabrication of $BaTiO_3$–$CoFe_2O_4$ (BTO–CFO) VANs and demonstrated the cross-control of ferroelectrics and magnetism from BTO perovskite and CFO spinel, respectively.[47] The elastic interaction of BTO and CFO at the vertical epitaxial interfaces facilitated a strong coupling between the electrical polarization and magnetic order, leading to magnetoelectric properties. Motivated by the promising magnetoelectric coupling of this classic multiferroic BTO–CFO system, a vast number of classic multiferroic VANs such as $PbTiO_3$–$CoFe_2O_4$, $BiFeO_3$–$CoFe_2O_4$, $BiFeO_3$–Sm_2O_3, $BiFeO_3$–Eu_2O_3, and $BiFeO_3$–$BaZrO_3$ have been widely studied ever since.[37,38,48–50] The remarkable functionalities of some of the multiferroic VAN systems are tabulated in Table I.

V. HIGHLIGHTS OF RECENT WORK ON OXIDE–OXIDE FERROELECTRIC VANS

A. Strain-, interface-, and defect-driven ferroelectric related functionalities

Dynamic polarization in the classic ferroelectric VAN has not been widely studied. However, dynamic polarization (polarization retention) has been studied in BSTO–SmO VAN films.[39] The ultimate aim of high polarization retention (either thermal or temporal) is to achieve infinite switching without degradation. However, polarization retention is limited by depolarization, inhomogeneous field distributions, defects and thermal depolarization, or back-switching of the poled state.[51,52] Figure 3(a) shows enhanced thermal polarization retention, $R(T)$, of BSTO–SmO VAN films as the SmO fraction, x, is increased. Such a phenomenon aligns with the manifestation of a high density of vertical interfaces (TbIn.$^{-2}$) between the BSTO nanopillars and SmO matrix.[39] These vertical interfaces not only act as surfaces for ferroelectric domains to nucleate but also act as domain pinning centers. This is distinctive because the domain motion can be confined and, simultaneously, the polarizations are retained for multiple switching cycles at elevated temperatures. Apart from dynamic polarization, a high P_r of 12.1 μC cm^{-2} (3× greater than that of the standard BSTO films) and d_{33} of 88.1 pm V^{-1}–81.4 pm V^{-1} up to 120 °C were achieved in the BSTO–SmO VANs.

In terms of recent T_c enhancements and strain control effects, this has been effectively demonstrated in $SrTiO_3$–Sm_2O_3 (STO–SmO) with T_c raised to >300 °C, the highest ever reported for T_c in STO [Fig. 3(b)].[36] In addition, in this system, a trade-off between dielectric tunability and loss is mitigated. A high dielectric tunability (49%) and low tangent loss (≤0.01) were achieved. This is desirable for impedance in high-power phase shifters and accelerators. The highest CQF reported (>2800), this factor integrating tunability and loss as a figure-of-merit, was reported in these STO–SmO VANs.

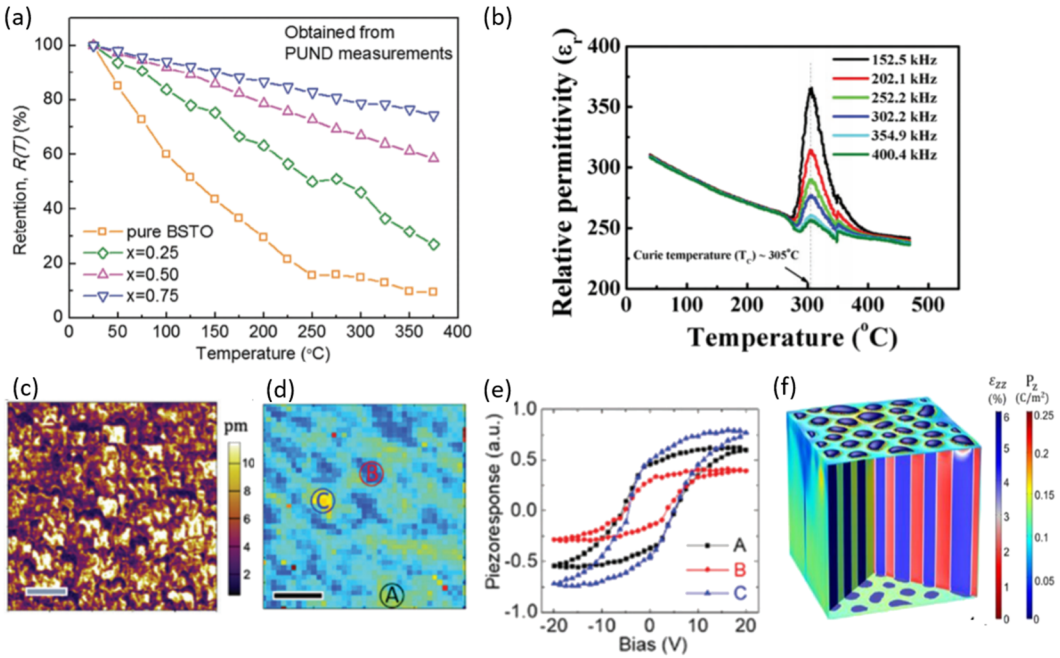

FIG. 3. BSTO–SmO, STO–SmO and STO–MgO VANs and their ferroelectric and dielectric properties. (a) Temperature dependence of polarization retentions of the BSTO–SmO VANs with different SmO fractions, x. Reproduced with permission from Lee *et al.*, Adv. Mater. Interfaces **4**(15), 1700336 (2017). Copyright 2017 WILEY-VCH.[39] (b) Temperature dependence of relative permittivity of the STO–SmO VAN at different frequencies, demonstrating an increment of T_c up to 305 °C. Reproduced with permission from Sangle *et al.*, Nanoscale **10**(7), 3460 (2018). Copyright 2018 The Royal Society of Chemistry.[36] (c) PFM image, (d) polarization switching mapping, and (e) piezo-response at locations A, B, and C of the STO–MgO VAN with scale bars of 200 nm. The existence of ferroelectricity in the STO–MgO VAN is consistent with (f) out-of-plane strain, ε_{zz}, distribution and polarization P_z obtained from phase field modeling. Reproduced with permission from Enriquez *et al.*, Nanoscale **12**(35), 18193 (2020). Copyright 2020 The Royal Society of Chemistry.[53]

Furthermore, to the STO–SmO VANs mentioned above, more recent work on $SrTiO_3$–MgO (STO–MgO) VANs[53] has shown room temperature ferroelectricity. Phase field modeling was performed to predict strain induced ferroelectricity in STO–MgO theoretically, followed by local *in situ* characterizations via piezoresponse force microscopy (PFM). Figures 3(c)–3(f) show the signature ferroelectricity of STO–MgO, also cross-checked by piezoresponse force microscopy (PFM), which shows the spatial resolution and functional ferroelectric response. Inhomogeneous polarization of the STO–MgO films stemming from a strain induced ferroelectric STO fraction and non-ferroelectric MgO nanopillars was resolved via polarization switching mapping, local hysteresis piezo-response loops at A, B, and C sites, and phase field modeling. Optical second harmonic generation (SHG) also provided the perfect complement for probing ferroelectricity in STO–MgO VANs due to its sensitivity toward C4v symmetry.

B. Ferroelectric–ferromagnetic couplings in multiferroic VANs

Recently, the popular multiferroic VAN system, BTO–CFO, has been revisited by Chen *et al.*[54] Figures 4(a) and 4(b) show the PFM amplitude mapping of non-ferroelectric CFO nanopillars (blue dots) embedded in a polarized BTO matrix (red area) and the discrepancy between the butterfly loops under zero and 2 kOe in-plane applied magnetic fields, indicating the presence of direct ME coupling or magnetic field control of ferroelectricity. The resulting direct ME coefficient of 390 $mVcm^{-1}Oe^{-1}$ at 8 kOe is higher than others (10 $mVcm^{-1}Oe^{-1}$–100 $mVcm^{-1}Oe^{-1}$). The work corroborates and expands on what Zavaliche *et al.* reported earlier, i.e., electric field induced magnetization reversal via magnetic force microscopy (MFM) in the BFO–CFO VANs.[55]

We now turn to a new room temperature multiferroic VAN comprised of ordered ferrimagnetic spinel α-$LiFe_5O_8$ (LFO) nanopillars in a matrix of ferroelectric perovskite $BiFeO_3$ (BFO).[56] As shown in Figs. 4(c)–4(e), the coexistence of ferroelectric polarization and magnetic order can be observed and compared via PFM phase poling, local PFM, and MFM images acquired at the same area. Both characterizations were carried out at room temperature. As we focus on the LFO nanopillars, their piezophase response is suppressed and, conversely, the magnetic response is enhanced. Apart from PFM and MFM, the magnetic switching induced by electric poling can be identified by x-ray magnetic circular dichroism (XMCD) as evidenced in the BFO–CFO and BTO–CFO systems.[57,58]

A key challenge to multiferroic VANs is the relatively high electrical conductivity in these systems arising from some conduction of the ferromagnetic (or ferrimagnetic) nanopillars, as well as the leaky ferroelectric matrix. Leakage can also arise from the vertical interfaces in the VAN films. Reduced leakage current density has been reported in both multiferroic VANs (BFO–CFO and BFO–EuO) and non-multiferroic VANs (BFO–SmO and BFO–BZO, as tabulated in Table I). The leakage current density of BFO–SmO VANs was reduced by three orders of magnitude in comparison with as-deposited pure BFO films.[37,38] Oxygen vacancies at the vertical interface, serving as donors, were believed to contribute mainly to the leakage reduction. Furthermore, tuning of vertical interface conduction has been described in the BFO–CFO VANs. Hsieh *et al.* reported a pathway to control local conduction due to oxygen vacancies at the BFO/CFO interface by a combination of conductive atomic force microscopy (c-AFM), PFM, and Kelvin force microscopy (KFM).[50] The local conduction was controllable by applying negative and positive tip biases on the as-grown BFO–CFO VANs (down polarization) once the BFO matrix was

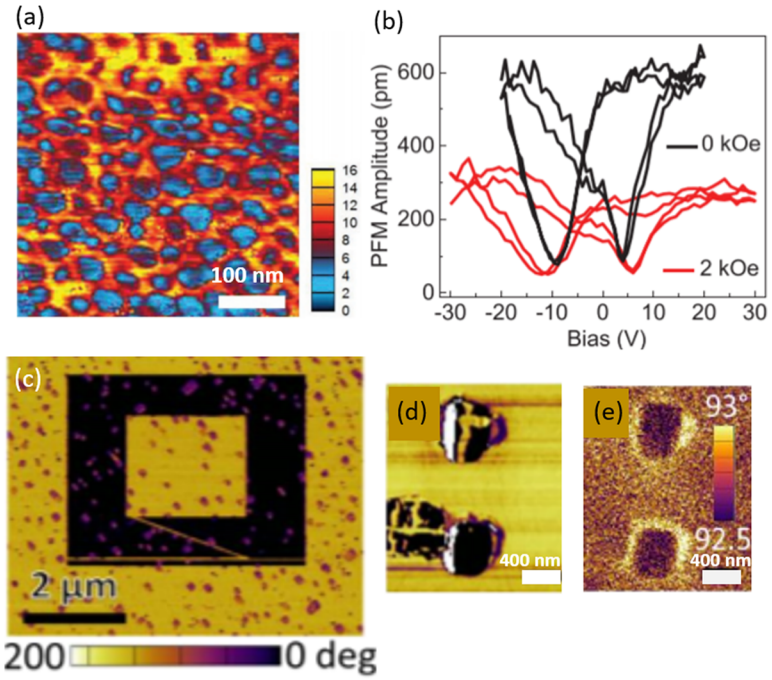

FIG. 4. Ferroelectricity–ferromagnetism coupling in the BTO–CFO and BFO–LFO VANs grown STO (100) substrates. (a) PFM amplitude mapping of the BTO–CFO VAN at a 2 kOe magnetic field and (b) amplitude–voltage butterfly loop of BTO–CFO VAN before and after the application of an external magnetic field of 2 kOe. Reproduced with permission from Chen *et al.*, Adv. Sci. **6**(19), 1901000 (2019). Copyright 2019 WILEY-VCH.[54] (c) PFM phase image taken after poling the BFO–LFO film using ±6 V. (d) Local PFM and (e) MFM acquired at the same area indicate the coexistence of ferroelectric and ferromagnetic whereby the piezo phase response of LFO nanopillars is suppressed and their magnetic response is enhanced, respectively. Reproduced with permission from Sharma *et al.*, Adv. Funct. Mater. **30**(3), 1906849 (2020). Copyright 2020 WILEY-VCH.[56]

pooled. Figure 5(a) illustrates that the positively charged oxygen vacancies (yellow dots) are attracted by the negative tip bias and accumulated on the top surface, thus suppressing the vertical conduction. After switching the polarization to upward [Fig. 5(b)], the conductive vertical interface diminishes as evidenced by the KFM image with a negative surface potential.

In parallel to the control of vertical conduction in BFO–CFO VANs, intriguing topological domain switching dynamics of BFO nanodomains has attracted broad attention.[59,60] Figure 5(c) shows the reconstructed polarization vector mapping of a BFO nanodomain from the PFM piezoresponse signal components using a MATLAB program. The BFO nanodomain exhibits a polarization configuration, which consists of stripe domains and convergent and divergent domain structures. Tian *et al.* found that the convergent and divergent domains were likely driven by the inhomogeneous strains exerted by vertical interface and substrate.[60] As a result, these inhomogeneous strains generate flexoelectric rotations and influence the polarization direction.

Strong leakage reduction in multiferroic VANs was also reported in the system $Na_{0.5}Bi_{0.5}TiO_3$–$CoFe_2O_4$ (NBT–CFO). The leakage was reduced by using the less leaky NBT ferroelectric and by creating a current-blocking *p*–*n* junction between the NBT and one of the electrodes. This system has enabled a strong converse (electric field control of magnetism) ME effect of 1.25×10^{-9} sm^{-1} to be achieved at room temperature.[61]

Research on new multiferroic VANs has been expanded to combine ferroelectric $BaTiO_3$ with multiferroic $YMnO_3$ ($YMnO_3$ is antiferromagnetic and concurrently exhibits geometric-driven ferroelectric) and ferrimagnetic yttrium iron garnet (YIG) $Y_3Fe_5O_{12}$.[62,63] The combinations prove the possibility to diversify the ME coupling for realizing RF/microwave devices with low noise and energy consumption. In addition, the newly developed $BaTiO_3$–$La_{0.7}Sr_{0.3}MnO_3$ (BTO–LSMO) VANs exhibit tunable anisotropic optical bandgaps, unveiling their potential toward an entirely new direction in non-linear optics.[64]

C. Spin-driven room temperature ferroelectric in $SmMnO_3$–$(Bi,Sm)_2O_3$

Type-II multiferroic materials have exquisitely coupled magnetic and ferroelectric orders via breaking of the inversion symmetry. However, no spontaneous room-temperature ferroic properties have been observed in the type-II multiferroics, orthorhombic $RMnO_3$, so far.[65,66]

Choi and co-workers incorporated stiff $(Bi,Sm)_2O_3$ nanopillars in a $SmMnO_3$ matrix, forming nanomaze VANs with clear phase separation in the plan-view scanning transmission electron microscopy (STEM) high-angle annular dark-field (HAADF) images [Figs. 6(a) and 6(b)].[43] These $(SmMnO_3)_{0.5}((Bi,Sm)_2O_3)_{0.5}$ (SMO–BSO) VANs demonstrated spin-driven ferroelectricity at

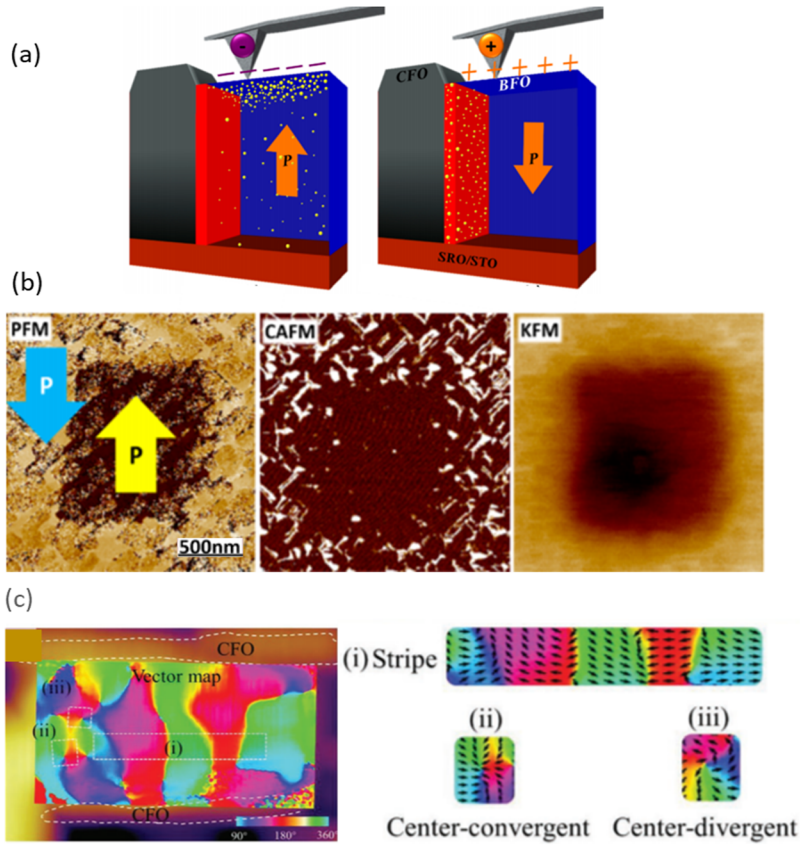

FIG. 5. Conduction modulation and domain switching in the BFO–CFO VANs on (100) $SrTiO_3$ and (110) $LaAlO_3$ substrates, respectively. (a) Schematic diagram showing that the local conduction due to oxygen vacancies at the BFO/CFO interface is controllable by applying negative and positive tip bias. The oxygen vacancies (yellow dots) are attracted by the negative tip bias and accumulated on the top surface of BFO. P represents the direction of ferroelectric polarization. Reproduced with permission from Hsieh *et al.*, ACS Nano **7**(10), 8627 (2013). Copyright 2013 American Chemical Society.[50] As evidenced by (b) PFM, CAFM, and KFM images: the out-of-plane phase orientation of BFO matrix is initially downward and possesses a conductive interface. Once the BFO is poled downward, the conductive vertical interphase as shown in the CAFM diminishes, whereas the KFM image depicts negative surface potential. (c) The domain switching of BFO is reconstructed by phase angle mapping, indicating (i) stripe domains, (ii) center-convergent domains, and (iii) center-divergent domains. Reproduced with permission from Tian *et al.*, Adv. Electron. Mater. **5**(7), 1900012 (2019). Copyright 2019 WILEY-VCH.[60]

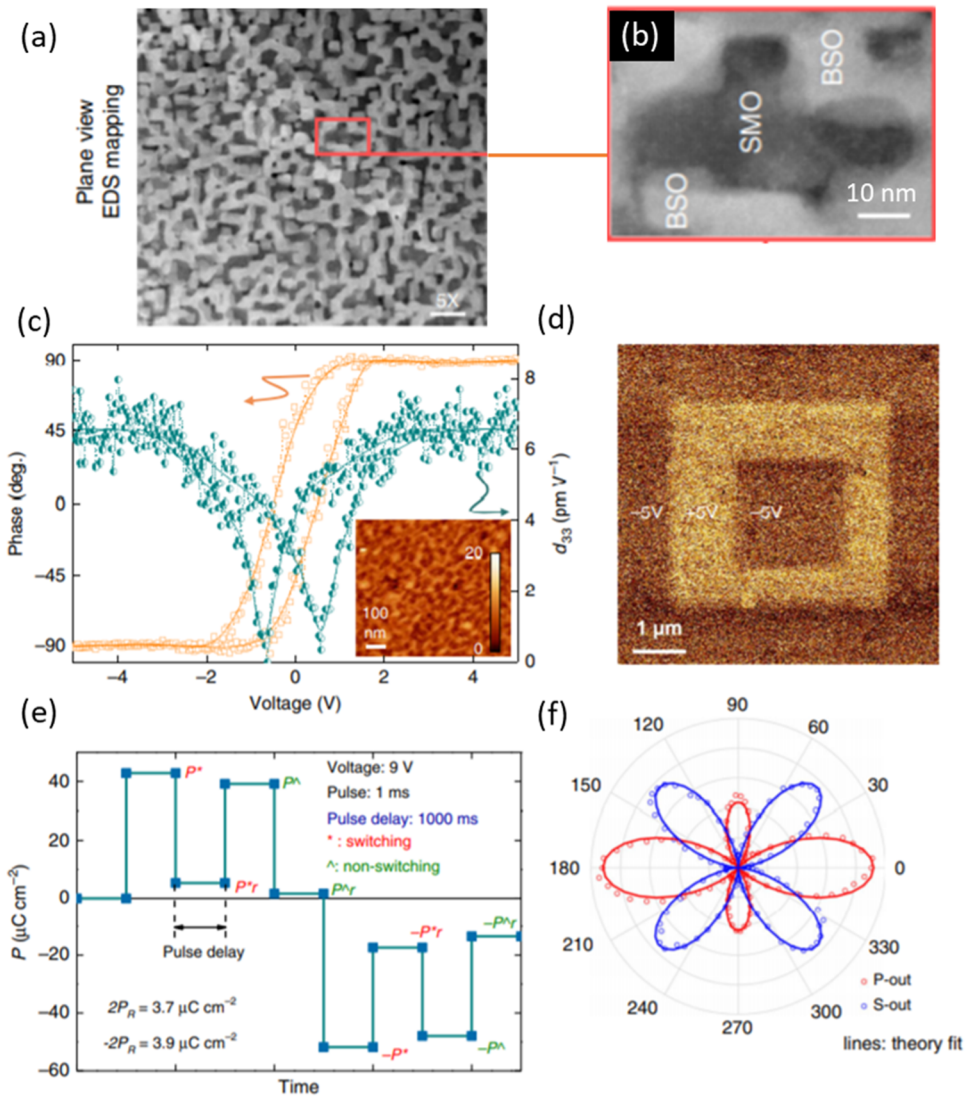

FIG. 6. SMO–BFO nanomaze VAN and room temperature and its intrinsic ferroelectricity. [(a) and (b)] Plan-view STEM-HAADF image of SMO–BFO VAN nanomaze structure over a wide area. A regular pattern of laterally connected BSO pillars in an SMO matrix is observed. (c) Amplitude (circle and blue) and phase (square and red) of the PFM signal as a function of bias voltage. The inset AFM image shows the surface morphology of the film. (d) PFM phase contrast after multiple ±5 V writing–rewritings at room temperature. The phase contrast remains after 24 h. (e) PUND measurements with 9 V (E = 500 kV cm^{-1}) for capturing both switching (*) and non-switching (') polarizations. The net switching polarization ($2P_R$) is ~3.9 μC cm^{-2}. (f) Room temperature optical SHG signals, which indicate p-wave (red) and s-wave (blue) of the second harmonic electric field with an incidence angle of 45°. Reproduced with permission from Choi *et al.*, Nat. Commun. **11**(1), 2207 (2020). Copyright 2020 Springer Nature.[43]

room temperature with a large d_{33} of 6.7 pmV^{-1}, 24 h remained PFM polings at ±5 V, and net switching remnant polarization ($2P_r$) of 3.9 μC cm^{-2} [Figs. 6(c)–6(e)]. A consistent result was observed from the SHG polar plots, indicating a breaking of centrosymmetry of SMO [Fig. 6(f)]. In addition, a clear ferromagnetic behavior was observed together with an enhanced ferromagnetic transition temperature (T_c) of 90 K and a saturation moment of 1.02 μ_BMn^{-1} (at 10 K). In contrast, bulk $SmMnO_3$ exhibits a ground state of paraelectricity with ferroelectric T_c < 40 K and A-type antiferromagnetism with a Néel temperature (T_N) of 60 K. The reason behind the T_c enhancement was the creation of large in-plane compression and out-of-plane tensile strains (−3.6% and +4.9%, respectively) exerted on the SMO, leading to the change in the Mn–O bond angle and length. As proven by density functional theory (DFT) calculations, the reduction of the Mn–O bond length and the increase in the Mn–O–Mn bond angle are in good agreement with the proposed mechanism of Mn–Mn exchange interactions. These enhanced interactions explain the room

temperature ferroelectric polarization and enhanced ferromagnetism in the SMO–BSO VANs.

VI. FUTURE OUTLOOK

Self-assembled oxide-based VAN thin films offer an interesting way toward achieving novel physical properties and functionality coupling ranging from ferromagnetic, ferroelectric, superconducting, and nonlinear optical effects as discussed above. These properties arise via coupling between charge, orbital, spin, and lattice degrees of freedom. However, due to the limited range of availability of structures in terms of crystallinity and morphology, a greater design flexibility and a structural complexity along with versatile growth techniques are needed for developing next generation integrated photonic and electronic devices. This can be achieved by several approaches such as designing VANs with unconventional phases, substituting one of the oxide phases with a metallic phase (oxide-metal nanocomposite), and fabricating self-assembled supercell-based nanocomposites. Each of these approaches is discussed in more detail in Secs. VI A–C.

A. Unconventional VANs

VANs also provide a platform to couple unconventional phases with vertical strain present along their interfaces to enhance their properties. Figure 7 shows a VAN structure composed of a new tetragonal tungsten bronze (TTB) phase, which is one of the most promising classes of ferroelectric materials.[67] The VAN structure shows the presence of a new TTB phase of $LiNb_6Ba_5Ti_4O_{30}$ (LNBTO), with a secondary phase, $LiTiO_2$ (LTO), that is present as vertical nanopillars embedded in the LNBTO matrix. Figure 7(a) presents the cross section STEM image showing the presence of a typical VAN structure. The main phase is determined to be LNBTO, while the darker contrast at the phase boundaries corresponds to LTO. This is further confirmed by the plan view STEM image in Fig. 7(b), showing a unique nanonecklace-like structure. Such an interesting structure combines the new TTB phase with the VAN design, resulting in enhanced multifunctional properties including ferroelectricity, anisotropic dielectric function, and strong optical nonlinearity.

Figure 7(c) shows the non-linear optical properties as measured using the SHG as a function of the polarization angle of the incident beam. The enhanced SHG signal can be attributed to (1) highly non-centrosymmetric crystal structure of the LNBTO phase and (2) the interface between LNBTO and LTO. Furthermore, Fig. 7(d) shows the ferroelectric hysteresis loop with low leakage, having P_s of 26 μC cm^{-2} and P_r of 8.1 μC cm^{-2} for a coercive field (E_c) of 74.6 kV cm^{-1}, which are comparable or higher than those of the constituent ferroelectric materials such as BTO or LNO. Such

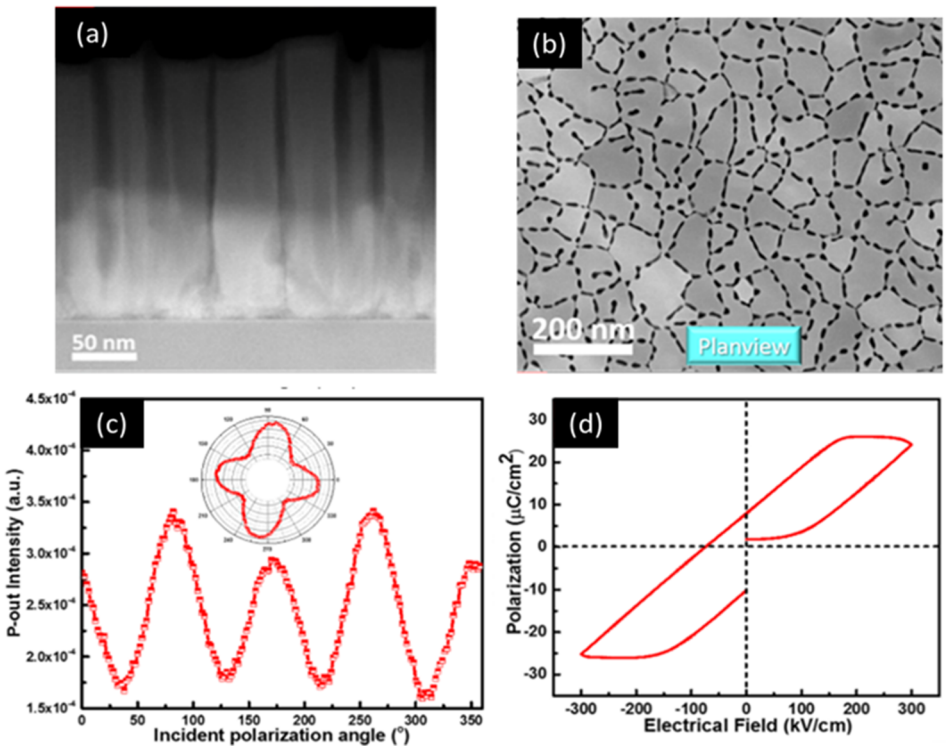

FIG. 7. $LiNb_6Ba_5Ti_4O_{30}$ (LNBTO)–$LiTiO_2$ (LTO) system. (a) Cross section and (b) plan-view STEM image of the LNBTO–LTO thin film nanocomposite showing the typical VAN structure with the darker phase corresponding to LTO, being segregated at the phase boundaries. (c) SHG intensity vs incident polarization angle with output polarization fixed at 0° (P-out) and (d) polarization hysteresis loop. Reproduced with permission from Huang *et al.*, ACS Appl. Mater. Interfaces **12**(20), 23076 (2020). Copyright 2020 American Chemical Society.[67]

unconventional VANs provide a new design pathway toward further multifunctionality and its compatible use with Si-based photonic devices.

B. Ferroelectric and multiferroic oxide–metal VANs

Recently, research has been focused on oxide–metal VAN hybrid nanostructures due to their practical device applications, which include aforementioned applications but in addition, optical metamaterials.[40,68–73] One of the first metallic-oxide VANs has been demonstrated by Vidal *et al.* in the Co–CeO_2 system with anisotropic magnetization having its easy axis along the OP direction.[74] Little work has been done by other groups on metallic-oxide VAN thereafter. However, in recent years, there have been numerous works. Figure 8(a) shows recent work of a representative two-phase Fe-BTO VAN with Fe nanopillars embedded within the BTO matrix.[75] Both the cross section and plan-view STEM images along with the energy dispersive spectroscopy (EDS) elemental mapping [Figs. 8(a1)–8(a3)] confirm the highly ordered growth of Fe nanopillars with a diameter of ~5 nm. Such an ordered structure can be attributed to the effective strain compensation along the vertical and lateral between the Fe and BTO matrix. The ferroelectric nature of the composite is shown by the PFM phase and amplitude switching curves in Fig. 8(a4). The presence of the Fe phase also contributes to the anisotropic ferromagnetic properties, thus classifying it as an artificial multiferroic material.

Greater design flexibility and structural complexity is required to develop next generation integrated electronic devices. This can be achieved through the three-phase nanocomposite design and growth. Figure 8(b) shows such a self-assembled ordered three-phase Au–BTO–ZnO nanocomposite, fabricated by depositing an Au–BTO VAN template layer followed by the BTO–ZnO VAN.[40] Both the cross section and plan-view STEM images along with the EDS elemental mapping shows a mix of Au particles, capping the ZnO nanowires, as well as Au pillars, embedded in the BTO matrix along with the highly ordered growth of both ZnO and Au phases. This unique "nanoman"-like structure is enabled by the combination of template-assisted Vapor Liquid Solid (VLS) and two-phase epitaxy growth mechanisms. Besides the interesting nonlinear and anisotropic optical properties, the three-phase nanocomposite is ferroelectric, which is confirmed by the PFM phase switching map, with a d_{33} piezoelectric coefficient of 19.4 pm V^{-1} greater than the two-phase BTO–ZnO VAN (~10 pm V^{-1}). Such multi-phase structures open new possibilities in design, growth, and engineering of other systems toward increased control over light–electron–matter interaction at the nanoscale.

C. Beyond VANs to self-assembled layered supercell structures

While VANs have been vastly explored for ferroelectric and multiferroic properties, there are also a new family of materials with a self-assembled layered supercell (LSC) structure that have room temperature multiferroic properties. These are of the form of self-assembled superlattices, as shown in Fig. 9. Such layered materials have been shown to be formed from Aurivillius

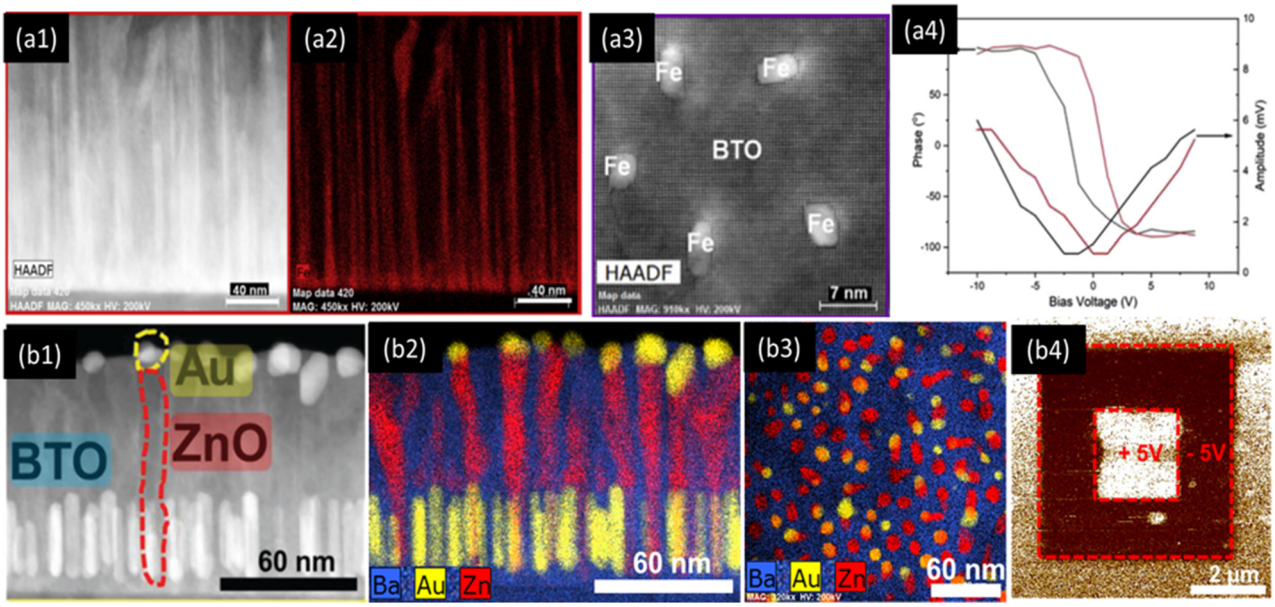

FIG. 8. (a) Fe–$BaTiO_3$ (BTO) system. (a1) Cross section STEM image and (a2) the corresponding EDS elemental map showing the Fe pillars embedded in the BTO matrix, (a3) plan-view STEM image showing the distribution of Fe pillars, and (a4) phase and amplitude switching curves measured using PFM. Reproduced with permission from Zhang *et al.*, Mater. Today Nano **11**, 100083 (2020). Copyright 2020 Elsevier Ltd.[75] (b) Au–$BaTiO_3$–ZnO ordered three phase nanocomposites. (b1) Cross section STEM image and (a2) the corresponding EDS elemental map showing the ordered Au pillars and Au nanoparticles capping the ZnO nanowires in a unique "nanoman" structure, (b3) plan-view STEM image showing the spatial ordered pillar distribution, and (b4) PFM phase switching map. Reproduced with permission from Misra *et al.*, Adv. Mater. **31**(7), 1806529 (2018). Copyright 2018 WILEY-VCH.[40]

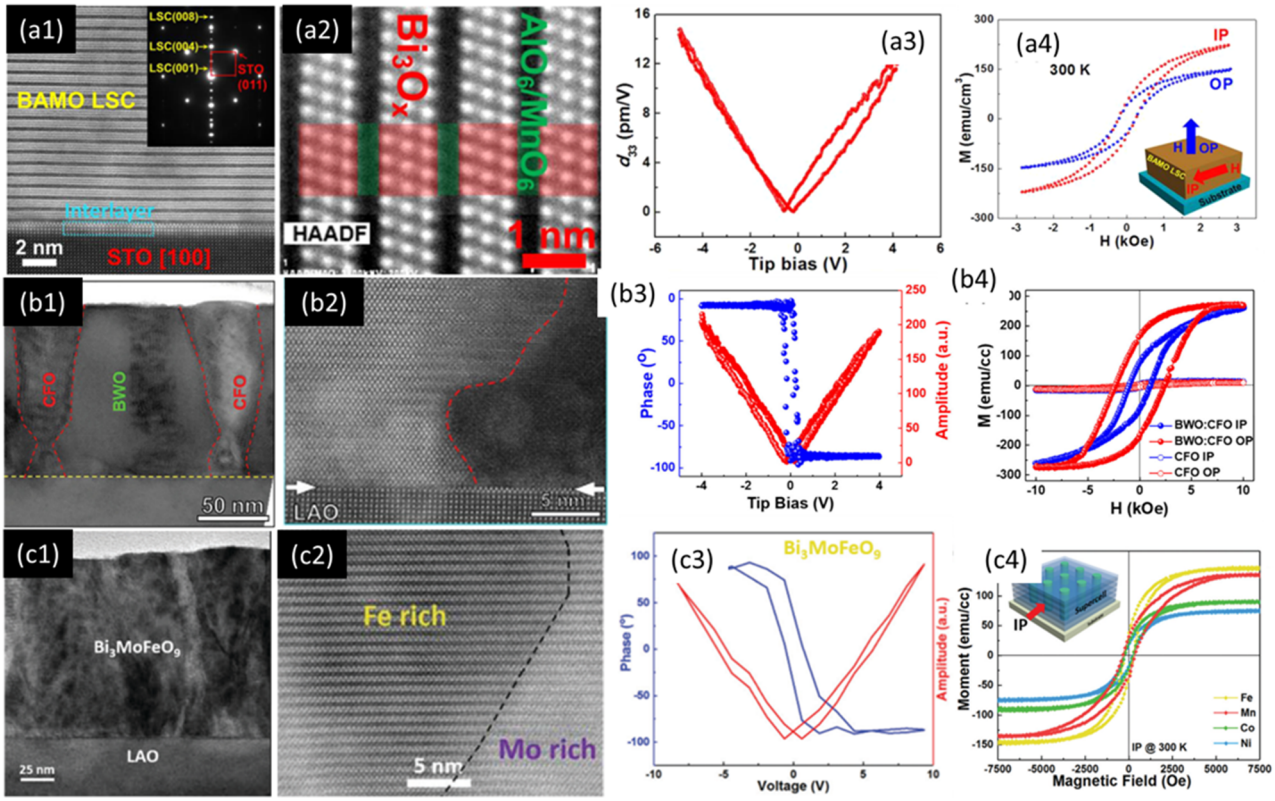

FIG. 9. (a) $Bi_2(AlMn)O_6$ (BAMO) layered supercell structure (LSC). (a1) Cross-sectional STEM image of the BAMO thin film deposited on STO (001) substrate. Inset shows the SAED pattern, (a2) HR-STEM image showing the LSC structure with a three-atom-thick Bi-based slab and one single Al/Mn based layer, (a3) piezoelectric coefficient d_{33} vs tip bias hysteresis loop at room temperature, and (a4) IP and OP magnetization hysteresis (M–H) loops of the BAMO LSC at 300 K. Reproduced with permission from Li *et al.*, Nano Lett. **17**(11), 6575 (2017). Copyright 2017 American Chemical Society.[32] (b) $BiWO_3$–$CoFeO_3$ (BWO–CFO) system. (b1) Cross section TEM image of the BWO–CFO system showing the CFO nanocones embedded in the layered BWO matrix, (b2) atomic-scale high-resolution STEM image of the BWO–CFO interface, (b3) amplitude and phase switching behavior of BWO–CFO, and (b4) IP and OP magnetization hysteresis loops of BWO–CFO and pure CFO at 300 K. Reproduced with permission from Wang *et al.*, Mater. Res. Lett. **7**(10), 418 (2019). Copyright 2019 Taylor and Francis.[78] (c) $Bi_3MoM_TO_9$ (T = Fe, Mn, Co, and Ni) LSC system. (c1) Cross-sectional TEM image and (c2) HR-TEM image of the Bi_3MoFeO_9 thin film, (c3) phase (blue) and amplitude (red) switching curves, and (c4) in-plane magnetic hysteresis loops of $BMoM_TO$ films measured at 300 K. Reproduced with permission from Gao *et al.*, Nanoscale **12**, 5914 (2020). Copyright 2020 The Royal Society of Chemistry.[77]

and Ruddlesden–Popper phases, and these compositions have various applications in piezoelectricity, superconductivity, water splitting, and thermoelectricity. For ferroelectric and multiferroics, Bi-based layered oxide structures have been widely explored, including Bi_2FeMnO_6, Bi_2AlMnO_6, and Bi_2NiMnO_6. They show room temperature multiferroicity arising from the coupling of ferroelectricity from the lone-pair electrons of Bi cations and ferromagnetism, which arises from the coupled Mn–M (M = Fe, Al, and Ni) cations.[27,31–33,76] Figure 9 shows three different such LSC structures, namely, Bi_2AlMnO_6 (BAMO), Bi_2WO_6–$CoFe_2O_4$ (BWO–CFO), and Bi_3MoMO_9 (M = Fe, Mn, Co, Ni; BMMO), along with their multiferroic properties.[32,77,78]

Figures 9(a1)–9(c1) shows the STEM image of the three different Bi-based LSC structures: BAMO, BWO–CFO, and BMFO having lattice planes parallel to the substrate.[32,77,78] All the films show a highly epitaxial growth along the (00*l*) out-of-plane direction. Figures 9(a2)–9(c2) shows the high-resolution STEM (HR-STEM) images of the LSC structures. Interestingly, the BAMO structure shows the supercell structure with three-atom-thick Bi-based slab and one single Al/Mn based layer. BWO–CFO VANs presents a mix of LSC and VAN structure with the CFO phase being embedded as a "nanocone"-like structure in the layered BWO matrix. The BMFO VANs shows a LSC with domain boundaries separating the Fe-rich and Mo-rich domain, and the LSC structures show the presence of the Aurivillius phase consisting of alternating Bi–O layers and M–O layers.

Interestingly, all the LSC structures show a coupled ferroelectric [Figs. 9(a3)–9(c3)] and ferromagnetic response [Figs. 9(a4)–9(c4)], thereby characterizing them as multiferroics. All the films show a well-defined ferroelectric hysteresis loop measured locally using the PFM, while the ferromagnetic character is confirmed by the M–H curves. The inherent anisotropy in LSC is confirmed by the different IP and OP ferromagnetic response, which is attributed to the presence of magnetic elements. More interestingly, most of the LSC structures show a strong IP magnetic response possibly due to the easy IP magnetocrystalline axis for the layered

structure. Therefore, by combining an Aurivillius phase with an appropriate perovskite transition metal oxide, an alternative way to explore new materials systems using LSC structures is provided. This gives further flexibility in VAN design and property tuning.

VII. OUTLOOK

Regarding the future research directions, selected focus directions in the field of ferroelectric VANs are as follows: (1) Modulation of defects such as oxygen vacancies by carefully controlling the deposition parameters. Oxygen vacancy migration plays a very important role in the tuning the conductance and changing the resistive characteristics of the films, which are useful in practical applications such as memristor and neuromorphic computing devices.[79–81] Therefore, it is critical to carefully control the oxygen vacancy concentration by introducing dopants and changing the deposition conditions. (2) Having a non-centrosymmetric structure, ferroelectric materials can also be used in non-linear optical devices including applications such as low-loss waveguides, wavelength conversion, and electro-optic modulators.[82,83] The use of VAN design provides further design flexibility in terms of property and microstructure tuning by varying the lateral and vertical strain state in the film. However, such photonic device applications require uniform deposition over a larger area than that can be achieved with pulsed laser deposition (PLD). Therefore, alternate deposition techniques such as sputtering or chemical vapor deposition (CVD) should be also be explored for VAN growth for scaling up device fabrication. There is some progress in this direction already.[84,85] (3) Recently, various data science techniques and machine learning (ML) models have been developed in the field of text and data mining, molecular modeling and microscopy image analysis for the accelerated materials discovery, data-driven materials design, and gaining insights into the material synthesis parameter.[86–91] However, most of the ML tools developed are for specific material systems and mostly for single phase materials with challenges in the consideration of complex materials interfaces and heterostructures.[92–94] Therefore, similar techniques can be extended toward the exploration of future VAN systems including the two-phase and three-phase nanocomposites having interesting electrical, magnetic, and optical applications.

AUTHORS' CONTRIBUTIONS

This manuscript was written through contributions of all authors. O.J.L. and S.M. contributed equally. All authors have given approval to the final version of the manuscript.

ACKNOWLEDGMENTS

O.J.L. acknowledges the support from the Ministry of Education, Malaysia, under the Fundamental Research Grant Scheme (Grant No. FRGS/1/2018/STG07/UMT/02/7). S.M. and H.W. acknowledge the support from the U.S. National Science Foundation for the VAN processing, characterization (Grant Nos. DMR-1565822 and DMR-2016453), and device related efforts (Grant No. ECCS-1902644). J.L.M.-D. acknowledges the Royal Academy of Engineering (Grant No. CIET1819-24), the Leverhulme Trust (Grant No. RPG-2015-017), EPSRC (Grant Nos. EP/N004272/1, EP/T012218/1, EP/P007767/1, and EP/M000524/1), and the Isaac Newton Trust in Cambridge [minute 16.24(p) and Grant No. RG96474].

DATA AVAILABLITY

Data sharing is not applicable to this article as no new data were created or analyzed in this study.

REFERENCES

[1] A. Chen, Q. Su, H. Han, E. Enriquez, and Q. Jia, Adv. Mater. **31**(4), 1803241 (2019).
[2] C. Clavero, Nat. Photonics **8**(2), 95 (2014).
[3] S. Lee and J. L. MacManus-Driscoll, APL Mater. **5**(4), 042304 (2017).
[4] J. L. MacManus-Driscoll, M. P. Wells, C. Yun, J.-W. Lee, C.-B. Eom, and D. G. Schlom, APL Mater. **8**(4), 040904 (2020).
[5] N. A. Spaldin and R. Ramesh, Nat. Mater. **18**(3), 203 (2019).
[6] W. Zhang, R. Ramesh, J. L. MacManus-Driscoll, and H. Wang, MRS Bull. **40**(9), 736 (2015).
[7] J. Narayan and B. C. Larson, J. Appl. Phys. **93**(1), 278 (2002).
[8] J. L. MacManus-Driscoll, A. Suwardi, and H. Wang, MRS Bull. **40**(11), 933 (2015).
[9] N. Setter, D. Damjanovic, L. Eng, G. Fox, S. Gevorgian, S. Hong, A. Kingon, H. Kohlstedt, N. Y. Park, G. B. Stephenson, I. Stolitchnov, A. K. Taganstev, D. V. Taylor, T. Yamada, and S. Streiffer, J. Appl. Phys. **100**(5), 051606 (2006).
[10] L. W. Martin and A. M. Rappe, Nat. Rev. Mater. **2**(2), 16087 (2016).
[11] S. Cho, J.-W. Jang, L. Li, J. Jian, H. Wang, and J. L. Macmanus-driscoll, Chem. Mater. **28**, 3017 (2016).
[12] A. Kursumovic, E. Defay, O. J. Lee, C. F. Tsai, Z. Bi, H. Wang, and J. L. MacManus-Driscoll, Adv. Funct. Mater. **23**(47), 5881 (2013).
[13] O. Lee, S. A. Harrington, A. Kursumovic, E. Defay, H. Wang, Z. Bi, C.-F. Tsai, L. Yan, Q. Jia, and J. L. MacManus-Driscoll, Nano Lett. **12**(8), 4311 (2012).
[14] D. Damjanovic, N. Klein, J. Li, and V. Porokhonskyy, Funct. Mater. Lett. **03**(01), 5 (2010).
[15] S. Basov, C. Elissalde, Q. Simon, M. Maglione, C. Castro-Chavarria, T. H. de Beauvoir, S. Payan, K. Temst, V. Lazenka, V. Andrei Antohe, P. M. P. de Sá, D. Sallagoity, and L. Piraux, Nanotechnology **28**(47), 475707 (2017).
[16] Y. Choo, P. W. Majewski, M. Fukuto, C. O. Osuji, and K. G. Yager, Nanoscale **10**(1), 416 (2018).
[17] M. Fan, B. Zhang, H. Wang, J. Jian, X. Sun, J. Huang, L. Li, X. Zhang, and H. Wang, Adv. Mater. **29**, 1606861 (2017).
[18] N. M. Aimon, H. K. Choi, X. Y. Sun, D. H. Kim, and C. A. Ross, Adv. Mater. **26**(19), 3063 (2014).
[19] T. C. Kim, S. Ojha, G. Tian, S. H. Lee, H. K. Jung, J. W. Choi, L. Kornblum, F. J. Walker, C. H. Ahn, C. A. Ross, and D. H. Kim, J. Mater. Chem. C **6**(20), 5552 (2018).
[20] X. Sun, J. L. MacManus-Driscoll, and H. Wang, Annu. Rev. Mater. Res. **50**(1), 229 (2020).
[21] H.-J. Liu, W.-I. Liang, Y.-H. Chu, H. Zheng, and R. Ramesh, MRS Commun. **4**(2), 31 (2014).
[22] J. L. MacManus-Driscoll, P. Zerrer, H. Wang, H. Yang, J. Yoon, A. Fouchet, R. Yu, M. G. Blamire, and Q. Jia, Nat. Mater. **7**(4), 314 (2008).
[23] A. Chen, Z. Bi, Q. Jia, J. L. MacManus-Driscoll, and H. Wang, Acta Mater. **61**(8), 2783 (2013).
[24] S. A. Harrington, J. Zhai, S. Denev, V. Gopalan, H. Wang, Z. Bi, S. A. T. Redfern, S.-H. Baek, C. W. Bark, C.-B. Eom, Q. Jia, M. E. Vickers, and J. L. Macmanus-driscoll, Nat. Nanotechnol. **6**(8), 491 (2011).
[25] W. Li, R. Zhao, R. Tang, A. Chen, W. Zhang, X. Lu, H. Wang, and H. Yang, ACS Appl. Mater. Interfaces **6** (8), 5356 (2014).
[26] A. Chen, W. Zhang, F. Khatkhatay, Q. Su, C.-F. Tsai, L. Chen, Q. X. Jia, J. L. Macmanus-Driscoll, and H. Wang, Appl. Phys. Lett. **102**(9), 093114 (2013).
[27] A. Chen, H. Zhou, Z. Bi, Y. Zhu, Z. Luo, A. Bayraktaroglu, J. Phillips, E.-M. Choi, J. L. Macmanus-driscoll, S. J. Pennycook, J. Narayan, Q. Jia, X. Zhang, and H. Wang, Adv. Mater. **25**, 1028 (2013).

[28]E.-M. Choi, A. Di Bernardo, B. Zhu, P. Lu, H. Alpern, K. H. L. Zhang, T. Shapira, J. Feighan, X. Sun, J. Robinson, Y. Paltiel, O. Millo, H. Wang, Q. Jia, and J. L. MacManus-Driscoll, Science Advances **5**(4), eaav5532 (2019).
[29]J. Jian, X. Wang, L. Li, M. Fan, W. Zhang, J. Huang, Z. Qi, and H. Wang, ACS Appl. Mater. Interfaces **9**, 5319 (2017).
[30]J. Kim, Y. Kim, Y. S. Kim, and J. Lee, Appl. Phys. Lett. **80**, 3581 (2002).
[31]L. Li, P. Boullay, J. Cheng, P. Lu, X. Wang, G. Steciuk, J. Huang, J. Jian, X. Gao, B. Zhang, S. Misra, X. Zhang, K. Yang, and H. Wang, Mater. Today Nano **6**, 100037 (2019).
[32]L. Li, P. Boullay, P. Lu, X. Wang, J. Jian, J. Huang, X. Gao, S. Misra, W. Zhang, O. Perez, G. Steciuk, A. Chen, X. Zhang, and H. Wang, Nano Lett. **17**(11), 6575 (2017).
[33]S. Misra, L. Li, X. Gao, J. Jian, Z. Qi, D. Zemlyanov, and H. Wang, Nanoscale Adv. **2**, 315 (2020).
[34]X. Sun, J. Huang, J. Jian, M. Fan, H. Wang, Q. Li, J. L. Mac Manus-Driscoll, P. Lu, X. Zhang, and H. Wang, Mater. Horiz. **5**, 536 (2018).
[35]W. Zhang, M. Fan, L. Li, A. Chen, Q. Su, Q. Jia, J. L. MacManus-Driscoll, and H. Wang, Appl. Phys. Lett. **107**(21), 212901 (2015).
[36]A. L. Sangle, O. J. Lee, A. Kursumovic, W. Zhang, A. Chen, H. Wang, and J. L. MacManus-Driscoll, Nanoscale **10**(7), 3460 (2018).
[37]Z. Bi, J. H. Lee, H. Yang, Q. Jia, J. L. MacManus-Driscoll, and H. Wang, J. Appl. Phys. **106**(9), 094309 (2009).
[38]H. Yang, H. Wang, G. F. Zou, M. Jain, N. A. Suvorova, D. M. Feldmann, P. C. Dowden, R. F. DePaula, J. L. MacManus-Driscoll, A. J. Taylor, and Q. X. Jia, Appl. Phys. Lett. **93**(14), 142904 (2008).
[39]O. Lee, A. Kursumovic, Z. Bi, C.-F. Tsai, H. Wang, and J. L. MacManus-Driscoll, Adv. Mater. Interfaces **4**(15), 1700336 (2017).
[40]S. Misra, L. Li, D. Zhang, J. Jian, Z. Qi, M. Fan, H.-T. Chen, X. Zhang, and H. Wang, Adv. Mater. **31**(7), 1806529 (2018).
[41]S. Misra, D. Zhang, Z. Qi, D. Li, J. Lu, H.-T. Chen, and H. Wang, Cryst. Growth Des. **20**(9), 6101 (2020).
[42]L. Yan, Z. Xing, Z. Wang, T. Wang, G. Lei, J. Li, and D. Viehland, Appl. Phys. Lett. **94**(19), 192902 (2009).
[43]E.-M. Choi, T. Maity, A. Kursumovic, P. Lu, Z. Bi, S. Yu, Y. Park, B. Zhu, R. Wu, V. Gopalan, H. Wang, and J. L. MacManus-Driscoll, Nat. Commun. **11**(1), 2207 (2020).
[44]Y. Cheng, B. Peng, Z. Hu, Z. Zhou, and M. Liu, Phys. Lett. A **382**(41), 3018 (2018).
[45]X. Zhang, R. Xu, X. Gao, Y. Ji, F. Qian, J. Fan, H. Wang, W. Li, and H. Yang, J. Mater. Chem. C **8**(24), 8091 (2020).
[46]F. Khatkhatay, A. Chen, J. H. Lee, W. Zhang, H. Abdel-Raziq, and H. Wang, ACS Appl. Mater. Interfaces **5**(23), 12541 (2013).
[47]H. Zheng, J. Wang, S. E. Lofland, Z. Ma, L. Mohaddes-Ardabili, T. Zhao, L. Salamanca-Riba, S. R. Shinde, S. B. Ogale, F. Bai, D. Viehland, Y. Jia, D. G. Schlom, M. Wuttig, A. Roytburd, and R. Ramesh, Science **303**(5658), 661 (2004).
[48]J. Li, I. Levin, J. Slutsker, V. Provenzano, P. K. Schenck, R. Ramesh, J. Ouyang, and A. L. Roytburd, Appl. Phys. Lett. **87**(7), 072909 (2005).
[49]W. Zhang, A. Chen, Z. Bi, Q. Jia, J. L. MacManus-Driscoll, and H. Wang, Current Opin. Solid State Mater. Sci. **18**(1), 6 (2014).
[50]Y.-H. Hsieh, E. Strelcov, J.-M. Liou, C.-Y. Shen, Y.-C. Chen, S. V. Kalinin, and Y.-H. Chu, ACS Nano **7**(10), 8627 (2013).
[51]C. Lichtensteiger, S. Fernandez-Pena, C. Weymann, P. Zubko, and J.-M. Triscone, Nano Lett. **14**(8), 4205 (2014).
[52]A. Stamm, D. J. Kim, H. Lu, C. W. Bark, C. B. Eom, and A. Gruverman, Appl. Phys. Lett. **102**(9), 092901 (2013).
[53]E. Enriquez, Q. Li, P. Bowlan, P. Lu, B. Zhang, L. Li, H. Wang, A. J. Taylor, D. Yarotski, R. P. Prasankumar, S. V. Kalinin, Q. Jia, and A. Chen, Nanoscale **12**(35), 18193 (2020).
[54]A. Chen, Y. Dai, A. Eshghinejad, Z. Liu, Z. Wang, J. Bowlan, E. Knall, L. Civale, J. L. MacManus-Driscoll, A. J. Taylor, R. P. Prasankumar, T. Lookman, J. Li, D. Yarotski, and Q. Jia, Adv. Sci. **6**(19), 1901000 (2019).
[55]F. Zavaliche, T. Zhao, H. Zheng, F. Straub, M. P. Cruz, P.-L. Yang, D. Hao, and R. Ramesh, Nano Lett. **7**(6), 1586 (2007).
[56]Y. Sharma, R. Agarwal, L. Collins, Q. Zheng, A. V. Ievlev, R. P. Hermann, V. R. Cooper, S. Kc, I. N. Ivanov, R. S. Katiyar, S. V. Kalinin, H. N. Lee, S. Hong, and T. Z. Ward, Adv. Funct. Mater. **30**(3), 1906849 (2020).
[57]C. Schmitz-Antoniak, D. Schmitz, P. Borisov, F. M. F. de Groot, S. Stienen, A. Warland, B. Krumme, R. Feyerherm, E. Dudzik, W. Kleemann, and H. Wende, Nat. Commun. **4**(1), 2051 (2013).
[58]Y.-J. Chen, Y.-H. Hsieh, S.-C. Liao, Z. Hu, M.-J. Huang, W.-C. Kuo, Y.-Y. Chin, T.-M. Uen, J.-Y. Juang, C.-H. Lai, H.-J. Lin, C.-T. Chen, and Y.-H. Chu, Nanoscale **5**(10), 4449 (2013).
[59]H. Huyan, L. Li, C. Addiego, W. Gao, and X. Pan, Nat. Sci. Rev. **6**(4), 669 (2019).
[60]G. Tian, S. Ojha, S. Ning, X. Gao, and C. A. Ross, Adv. Electron. Mater. **5**(7), 1900012 (2019).
[61]R. Wu, A. Kursumovic, X. Gao, C. Yun, M. E. Vickers, H. Wang, S. Cho, and J. L. MacManus-Driscoll, ACS Appl. Mater. Interfaces **10** (21), 18237 (2018).
[62]G. Dong, Z. Zhou, X. Xue, Y. Zhang, B. Peng, M. Guan, S. Zhao, Z. Hu, W. Ren, Z.-G. Ye, and M. Liu, ACS Appl. Mater. Interfaces **9** (36), 30733 (2017).
[63]X. Gao, L. Li, J. Jian, H. Wang, M. Fan, J. Huang, X. Wang, and H. Wang, ACS Appl. Nano Mater. **1**(6), 2509 (2018).
[64]X. Gao, D. Zhang, X. Wang, J. Jian, Z. He, H. Dou, and H. Wang, Nanoscale Adv. **2**(8), 3276 (2020).
[65]T. Kimura, G. Lawes, T. Goto, Y. Tokura, and A. P. Ramirez, Phys. Rev. B **71**(22), 224425 (2005).
[66]M. Fiebig, T. Lottermoser, D. Meier, and M. Trassin, Nat. Rev. Mater. **1**(8), 16046 (2016).
[67]J. Huang, H. Wang, D. Li, Z. Qi, D. Zhang, P. Lu, H.-T. Chen, D. A. Yarotski, P.-T. Lin, X. Zhang, and H. Wang, ACS Appl. Mater. Interfaces **12**(20), 23076 (2020).
[68]N. Fang, H. Lee, C. Sun, and X. Zhang, Science **308**, 534 (2005).
[69]J. Huang, T. Jin, S. Misra, H. Wang, Z. Qi, Y. Dai, X. Sun, L. Li, J. Okkema, H.-T. Chen, P.-T. Lin, X. Zhang, and H. Wang, Adv. Opt. Mater. **6**, 1800510 (2018).
[70]J. Huang, X. Wang, X. L. Phuah, P. Lu, Z. Qi, and H. Wang, Mater. Today Nano **8**, 100052 (2019).
[71]S. Kawasaki, R. Takahashi, T. Yamamoto, M. Kobayashi, H. Kumigashira, J. Yoshinobu, F. Komori, A. Kudo, and M. Lippmaa, Nat. Commun. **7**, 11818 (2016).
[72]S. Misra, L. Li, J. Jian, J. Huang, X. Wang, D. Zemlyanov, J.-W. Jang, F. H. Ribeiro, and H. Wang, ACS Appl. Mater. Interfaces **10**, 32895 (2018).
[73]R. L. Paldi, X. Sun, X. Wang, X. Zhang, and H. Wang, ACS Omega **5**, 2234 (2020).
[74]F. Vidal, Y. Zheng, J. Milano, D. Demaille, P. Schio, E. Fonda, and B. Vodungbo, Appl. Phys. Lett. **95**(15), 152510 (2009).
[75]B. Zhang, J. Huang, B. X. Rutherford, P. Lu, S. Misra, M. Kalaswad, Z. He, X. Gao, X. Sun, L. Li, and H. Wang, Mater. Today Nano **11**, 100083 (2020).
[76]E. M. Choi, T. Fix, A. Kursumovic, C. J. Kinane, D. Arena, S. L. Sahonta, Z. Bi, J. Xiong, L. Yan, J. S. Lee, H. Wang, S. Langridge, Y. M. Kim, A. Y. Borisevich, I. MacLaren, Q. M. Ramasse, M. G. Blamire, Q. Jia, and J. L. MacManus-Driscoll, Adv. Funct. Mater. **24**(47), 7478 (2014).
[77]X. Gao, L. Li, D. Zhang, X. Wang, J. Jian, Z. He, and H. Wang, Nanoscale **12**, 5914 (2020).
[78]H. Wang, L. Li, J. Huang, X. Gao, X. Sun, and H. Wang, Mater. Res. Lett. **7**(10), 418 (2019).
[79]J.-Y. Chen, C.-W. Huang, C.-H. Chiu, Y.-T. Huang, and W.-W. Wu, Adv. Mater. **27**(34), 5028 (2015).
[80]F. Gul and H. Efeoglu, Ceram. Int. **43**(14), 10770 (2017).
[81]P. Hou, J. Wang, X. Zhong, and Y. Wu, RSC Adv. **6**(59), 54113 (2016).
[82]R. C. Alferness, IEEE Trans. Microwave Theory Tech. **30**(8), 1121 (1982).
[83]J. Leuthold, C. Koos, and W. Freude, Nat. Photonics **4**(8), 535 (2010).
[84]J. Gao, X. Wu, Q. Li, S. Du, F. Huang, L. Liang, H. Zhang, F. Zhuge, H. Cao, and Y. Song, Adv. Mater. **29**(16), 1605324 (2017).
[85]A. G. Wattoo, R. Bagheri, X. Ding, B. Zheng, J. Liu, C. Xu, L. Yang, and Z. Song, J. Mater. Chem. C **6**(32), 8646 (2018).

[86]K. T. Butler, D. W. Davies, H. Cartwright, O. Isayev, and A. Walsh, Nature **559**(7715), 547 (2018).
[87]S. V. Kalinin, B. G. Sumpter, and R. K. Archibald, Nat. Publ. Group **14**(10), 973 (2015).
[88]E. Kim, K. Huang, A. Saunders, A. McCallum, G. Ceder, and E. Olivetti, Chem. Mater. **29**(21), 9436 (2017).
[89]T. S. Qiu, X. Shi, J. F. Wang, Y. F. Li, S. B. Qu, Q. Cheng, T. J. Cui, and S. Sui, Adv. Sci. **6**, 1900128 (2019).
[90]V. Tshitoyan, J. Dagdelen, L. Weston, A. Dunn, Z. Rong, O. Kononova, K. A. Persson, G. Ceder, and A. Jain, Nature **571**(7763), 95 (2019).
[91]Y. Zhang and C. Ling, npj Comput. Mater. **4**(1), 25 (2018).
[92]J. C. Agar, Y. Cao, B. Naul, S. Pandya, S. van der Walt, A. I. Luo, J. T. Maher, N. Balke, S. Jesse, S. V. Kalinin, R. K. Vasudevan, and L. W. Martin, Adv. Mater. **30**, 1800701 (2018).
[93]L.-Q. Chen, J. Am. Ceram. Soc. **91**(6), 1835 (2008).
[94]Q. Li, C. T. Nelson, S.-L. Hsu, A. R. Damodaran, L.-L. Li, A. K. Yadav, M. McCarter, L. W. Martin, R. Ramesh, and S. V. Kalinin, Nat. Commun. **8**(1), 1468 (2017).
[95]M. J. Chen, X. K. Ning, S. F. Wang, and G. S. Fu, RSC Adv. **7**(61), 38231 (2017).